Nanometallic antenna assisted amorphous silicon waveguide integrated bolometer for mid-infrared

Yangbo Wu[1], **Zhibo Qu**[1], **Ahmed Osman**[1], **Chen Wei**[1], **Wei Cao**[1], **Antulio Tarazona**[2], **Swe Zin Oo**[2], **Harold M.H. Chong**[2,3], **Otto L. Muskens**[4], **Goran Z. Mashanovich**[1,5], **and Milos Nedeljkovic**[1,*]

[1] *Optoelectronics Research Centre, University of Southampton, University Road, Southampton, Hampshire SO17 1BJ, United Kingdom*
[2] *School of Electronics and Computer Science, University of Southampton, University Road, Southampton, Hampshire SO17 1BJ, United Kingdom*
[3] *Japan Advanced Institute of Science and Technology, Ishikawa 932-1211, Japan*
[4] *School of Physics and Astronomy, University of Southampton, University Road, Southampton, Hampshire SO17 1BJ, United Kingdom*
[5] *School of Electrical Engineering, University of Belgrade, 11120 Belgrade, Serbia*
[*] *Corresponding author: M.Nedeljkovic@soton.ac.uk*

Compiled December 3, 2020

Bolometers are thermal detectors widely applied in the mid-infrared (MIR) wavelength range. MIR silicon photonics is a promising platform for emerging applications, e.g. in optical sensing, for its low cost and high volume manufacturing potential. In an integrated sensing system on chip, a broadband scalable bolometer absorbing the light over the whole MIR wavelength range could play an important role. In, this work, we have developed a waveguide-based bolometer operating in the wavelength range of 3.72 - 3.88 μm on the amorphous silicon (a-Si) platform. Significant improvements in the bolometer design result in a 20x improved responsivity compared to earlier work on SOI. The bolometer offers 24.62 % change in resistance per milliwatt of input power at 3.8 μm wavelength. The thermal conductance of the bolometer is 3.86 $\times$ 10^{-5} W/K and an improvement as large as 3 orders magnitude may be possible in the future through redesign of the device geometry.

http://dx.doi.org/10.1364/ao.XX.XXXXXX

The mid-infrared (MIR) wavelength region is attractive for many applications such as chemical and biological sensing, industrial process control, astronomy and free-space communications [1, 2]. Amongst these potential applications, chemical sensing attracts the most attention, because a number of molecules have unique absorption bands in the "functional group" and "molecular fingerprint" regions (2.5 - 20 μm) [3, 4]. Over the past decade, silicon photonics research has been extended from the near-infrared (NIR) to the MIR, because the common material in silicon photonics, silicon (Si), has low absorption loss up to the wavelength of 8.5 μm [5], and germanium (Ge) can be used to extend the transmission up to 14 μm. Low loss MIR waveguides based on Si and Ge have been developed [6–9]. On the other hand, amorphous silicon (a-Si) which has advantages of low-cost and CMOS compatible has been investigated in the last several years. It also has potential to be applied in MIR [10, 11].

In an integrated photonics system, detectors play an important role. Several integrated MIR detectors have been demonstrated [12–15]. Most of these detectors are photon detectors and the main limitation of this type of detectors is that the operating wavelength range is material specific and therefore not scalable over the whole MIR wavelength range. Apart from the photon detectors, the thermal detectors are another important class of detectors in the MIR field. One major advantage of the thermal detector is the wavelength independence when an absorption mechanism is used that is wavelength independent [16]. The bolometer is a widely used thermal detector. In the last year, we have developed the antenna-assisted integrated waveguide-based bolometers on the SOI platform [17, 18]. The antenna-assisted bolometer is based on a rod-antenna cluster interacting with the incident light and exciting the localised surface plasmon resonance (LSPR) to absorb the incident light. In the first-generation bolometers, an a-Si arm created by Ge ion implantation acted as the thermometer. However, in this design, the high thermal conductivity of the surrounding crystalline silicon (c-Si) resulted in a high heat leak which strongly limited the responsivity of the bolometer to values at around 1 %/mW. Compared with c-Si, a-Si has an advantage of low thermal conductivity. Therefore, it can better confine the heat in a localised region and achieve a higher temperature change. In the current work, we developed the bolometer on the a-Si platform to significantly improve its performance.

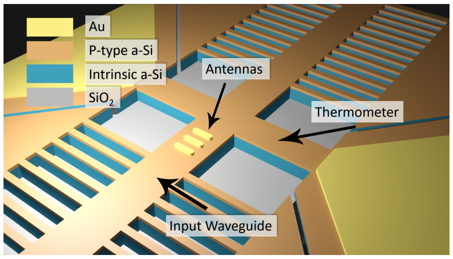

Fig. 1. Diagram of the structure of the designed bolometer based on the a-Si platform.

The waveguide-based bolometer is based on the a-Si platform. The geometry of the bolometer is shown in Figure 1. a-Si is a common material for bolometers. It has a high temperature coefficient of resistance (TCR) of 2.5 %/K [19] and also a low thermal conductivity of 2.2 W/(m·K) [20], hence it can confine generated heat in a localised region. However, the resistivity of intrinsic a-Si is extremely high (5 $\times 10^{10}$ Ωcm [21]), hence a change in resistance is difficult to measure. Therefore, a heavily doped p-type a-Si layer is introduced on top of the waveguide in order to reduce the resistance. On the other hand, the doped a-Si would also introduce more absorption loss. To balance the resistivity and the absorption loss, the a-Si platform includes a 400 nm thick intrinsic a-Si layer and a 100 nm thick p-type a-Si layer on the top. The heavily doped a-Si layer could be etched after deposition so that it is present only in the bolometer region, but in this demonstration it is left covering all of the waveguides, to reduce the fabrication complexity.

The a-Si bolometer is based on a 1.3 μm wide waveguide core with sub-wavelength grating (SWG) cladding which are designed for TE only[22]. This kind of waveguide has the potential to be suspended to realise a stronger thermal insulation. In the bolometer, three nanometallic optical rod antennas are fabricated on the surface of the waveguide to as the absorber [17]. The dimensions of each antenna is 540 nm length, 160 nm width and 20 nm thickness, as obtained using e-beam lithography and lift-off. We use gold as the material of choice for its excellent plasmonic properties and chemical inertness. These antennas absorb the incident light and heat up the localised area including the thermometer arm which is positioned close to these antennas (Figure 1). The thermometer is a strip of 1 μm wide and 6.3 μm long, which is aligned perpendicular to the waveguide between two contact pads (see Figure 1). In theory, the temperature change in the bolometer is described as [16]

$$\Delta T = \frac{\varepsilon \Phi_0}{(G_{th}^2 + \omega^2 C_{th}^2)^{1/2}} \tag{1}$$

where ΔT is the temperature change, ε is the absorbing efficiency of detector, Φ_0 and ω are the optical power amplitude and the modulating frequency of incident radiation, C_{th} is the thermal capacitance of the detector and G_{th} is the thermal conductance to the surroundings.The resistance change in the thermometer caused by the localized heating is measured by applying a constant voltage across the two contact pads on the two sides of the thermometer and monitoring the change in current (Figure 1).

To predict the thermal profile in the bolometer, a simulation model was built using the COMSOL Multiphysics software. Although the absorption rate in these three antennas are slightly different and dependent on the wavelength, in our thermal simulation the three antennas are considered as a uniform heat source , which provides an accurate description given the proximity of the three sources compared to the thermal diffusion length as discussed below. The background environment temperature is set as 293.15 K and the convective heat transfer coefficient of air is set as 5 W/(m^2·K) [23]. The properties of the materials are shown in Section B of the supplementary document.

For the heating power of 1 mW in the antennas, the thermal simulation produces the results shown in Figure 2. From Figure 2a, the temperature in the localised region around the antennas is over 600 K (350 °C). The temperature decays quickly away from the antennas. In the cross-section of the thermometer (Figure 2b), the temperature of the waveguide core is 350 K, and the temperature in at the far ends of the bolometer (close to the contacts) is 300 K. Although the antenna region is the heating centre with extremely high temperature, there is a 1.5 μm offset between the antennas and the thermometer, which was introduced in order to reduce the light scattering from the thermometers. One advantage of a-Si is the low thermal conductivity. The heat generated in the antennas is confined in a tiny micrometer region. To compare the materials of c-Si and a-Si, a bolometer with a similar structure but based on the c-Si platform with an a-Si thermometer has been simulated. In Figure 2c, the temperature in the region immediately around the antennas is only 311 K. Compared with the a-Si waveguide, the c-Si waveguide conducts the heat to the surrounding quickly. In the cross section of the thermometer (Figure 2d), the temperature of the waveguide core is 301 K. It is clear that with the same heating power in the antennas, the c-Si waveguide bolometer has a lower temperature change in the thermometer.

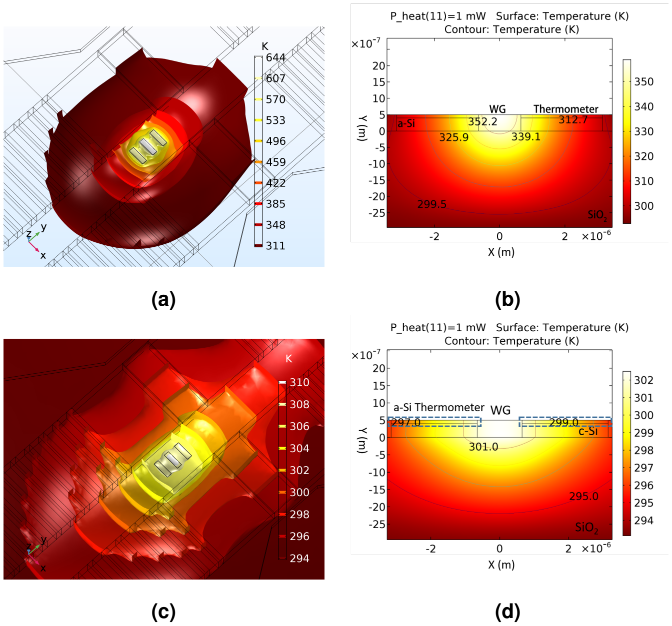

(a) (b)

(c) (d)

Fig. 2. Thermal profile of (a) the whole a-Si bolometer and (b) the thermometer cross section in the simulation. (The temperature of the white region at the outside of the bolometer is lower than 311 K which is out of the coulor scale.) Thermal profile of (c) the c-Si bolometer with the a-Si thermometer and (d) the cross section of the thermometer in the simulation. The dash rectangles are a-Si thermometers.

Figure 3 plots the simulated temperature response to varying

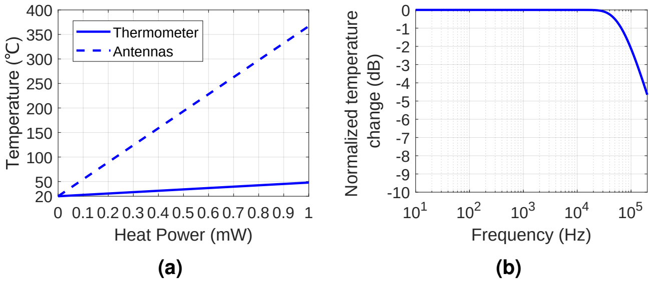

(a) (b)

Fig. 3. (a) Average temperature in the antennas and thermometers versus the heating power in the antennas in the simulation. (b) The normalised temperature change with respect to the modulating frequency of the heating power in the simulation.

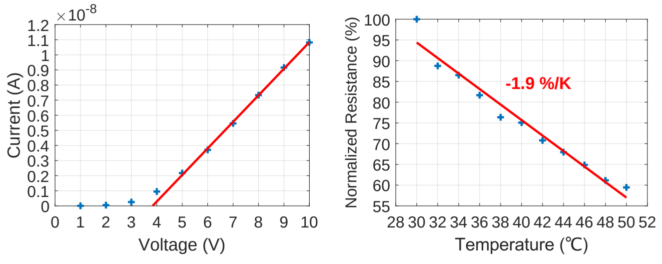

(a) (b)

Fig. 4. (a) The IV curve of the bolometer at the temperature of 30 °C. (b) The normalised resistance of the bolometer versus the temperature of the sample.

heating power, and the frequency response of the bolometer in the simulation. It is clear that the temperature in the antennas is much higher than the temperature in the thermometer due to the low thermal conductivity of a-Si. On the other hand, the antennas are not only absorbing but also reflecting and scattering the incident light. In the simulation, the absorption of three antennas is 70 % [17]. However, due to fabrication errors in the antennas, the absorption coefficient is usually less than the simulation result. Assuming that the absorbing rate of antennas is 50 %, the responsivity of the bolometer is 13.97 K/mW. Under the stationary simulation, the frequency-dependent term, $\omega^2 C_{th}^2$, can be ignored. Then, according to the calculation, the thermal conductance, G_{th}, is 3.58×10^{-5} W/K. From Figure 3b, the 3 dB bandwidth is 129.57 kHz, therefore the thermal capacitance is 7.62×10^{-11} J/K.

The fabrication begins with preparing a bulk silicon sample. To get the designed a-Si on insulator sample, 3 μm SiO_2 was deposited by plasma enhanced chemical vapor deposition (PECVD) firstly. After that, 400 nm intrinsic a-Si and 100 nm p-type a-Si were deposited by hot wire chemical vapor deposition (HWCVD) on the sample sequentially. In the p-type a-Si deposition, the gas ratio between B_2H_6 and SiH_4 is 10 : 40 sccm. Then, the passive devices, waveguides and gratings, were patterned on the sample. After that, 200 nm thick Au contact pads were deposited on the sample, with a 10 nm thin Cr layer between the Si and Au used as an adhesion layer. Finally, the optical antennas (composed of 1 nm thick Cr as the adhesion layer and 20 nm Au) were deposited. The sketch of the fabrication processes flow is presented in Section 1 of the supplementary document.

The experimental setup is similar to that described in [17], where the DC source was upgraded to Keithley 6487. Firstly, The waveguide propagation loss has been measured by the cut-back method and the loss is 94 dB/cm. In this demonstration this high loss is avoided by using a short input waveguide length (< 1mm). The high loss does not significantly reduce the performance of the bolometer itself because of the very short length of the bolometer. In the future, the a-Si bolometer could be integrated with a c-Si waveguide based sensing circuit on the SOI platform. Then, the resistance of the bolometer was measured by heating up the whole sample to different temperatures using a Peltier stage. Figure 4a presents the IV curve of the bolometer at 30 °C. It illustrates that there is a Schottky contact between the contact pad and the p-type a-Si. By fitting the linear region of the IV curve, the resistance is found to be $5.69 \times 10^8 \Omega$. Figure 4b plots a normalized resistance with respect to the temperature. Assuming the sheet resistance of p-type a-Si is dominant, the TCR of the p-type a-Si is -1.9 %/K from the linear fitting.

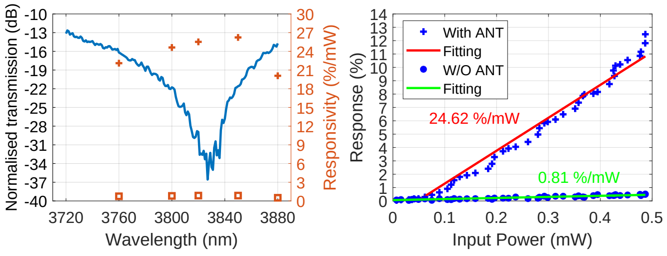

(a) (b)

Fig. 5. (a) The blue line is the normalised transmission spectrum of the bolometer. The plus sign and square marks are the responsivity of the bolometer with and without antennas, respectively.(b) Response of bolometers with and without the antennas versus the input power at 3.8 μm wavelength and 400 Hz chopping frequency.

The normalized transmission spectrum of the antennas is shown in Figure 5a. The transmission of the antennas is less than -10 dB over the 3.72 - 3.88 μm wavelength range. At the wavelength 3820nm, the transmission is even less than -30 dB. This result illustrates that the antennas have a broadband response, with a 3 dB bandwidth greater than 160 nm. In the response measurement, we measured the current change with a constant voltage instead of measuring the resistance of the bolometer. To investigate the enhancement from the antennas, the bolometer without the antennas is measured as the reference. Figure 5b plots the response versus the input power of the bolometers with and without the antennas at the wavelength of 3.8 μm and the chopping frequency of 400 Hz. From the linear fitting, the responsivity of the bolometer is 24.62 %/mW and the reference bolometer has a responsivity of only 0.81 %/mW. Therefore, the antennas introduce a 14.83 dB enhancement on the responsivity of the bolometer. In addition, the responsivities of bolometer with and without antenans at different wavelengths are shown in Figure 5a.

To test the frequency response of the bolometers, the response of the bolometers versus the chopping frequency was scanned. Figure 6a plots the responsivity of the bolometer with the antennas versus the chopping frequency. The responsivity of the bolometer doesn't show an obvious attenuation up to 1 kHz, which is the maximum frequency limit of the chopper. It indicates that the term of the thermal conductance to the surroundings in Equation 1, G_{th} predominantly limits the temperature change in the bolometer. Assuming the absorption coefficient is 50 %, the thermal conductance of the bolometer is 3.86×10^{-5} W/K, which matches the simulation result. On the other hand, a free-space coupled bolometer (forming part of a camera array) with a thermal conductance of 2.38×10^{-8} W/K has been reported in [24]. Suspension is an effective method for improving the thermal insulation [17]. In the simulation shown in Section 2 of the supplementary document, the thermal conductance after the suspension is reduced to 3.46×10^{-6} W/K. Therefore, there is still a high heat loss through the waveguide. It indicates that still responsivity improvement of 2 - 3 orders of magnitude may be possible in the future through redesign of the device geometry. Meanwhile, the noise with respect to the chopping frequency is plotted in Figure 6b. In the frequency range from 50 Hz to 10 kHz, the noise does not decrease quickly as frequency increases and the mean value of the noise is only $0.0247\ \%/\sqrt{Hz}$. The noise equivalent power (NEP) of the bolometer at 400 Hz is $10.4\ \mu W/\sqrt{Hz}$. (The detail of NEP calculation is shown in

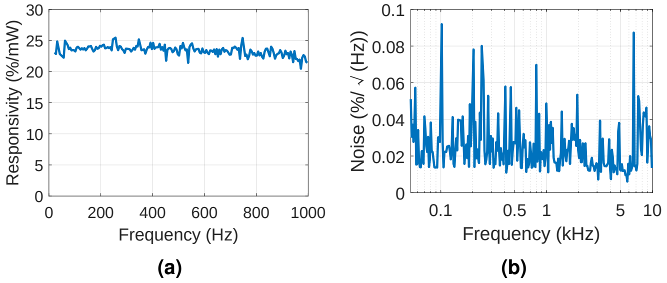

(a) (b)

Fig. 6. (a) Responsivity and (b) noise of the bolometer versus the chopping frequency.

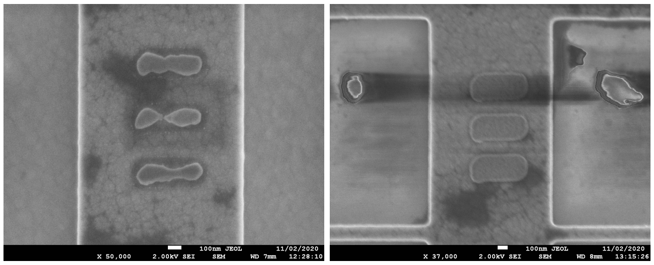

(a) (b)

Fig. 7. SEM images of the antennas of bolometers that (a) have and (b) have not been exposed to a high input power.

Section 3 of the supplementary document.)

To further investigate the response of the bolometer with a high input power, a light with a power of 1.2 mW is coupled into the bolometer. At these high input powers, we observe an irreversible reduction in the responsivity from 24.62 %/mW down to 7.26 %/mW. Figure 7a and 7b present scanning electron microscopy (SEM) images of the antennas of bolometers that have and have not been exposed to a high input optical power. It is clearly visible that the antennas have been damaged after coupling a high input power up to 1.2 mW. According to the high responsivity, 24.62 %/mW and the TCR, -1.9 %/K, the temperature change in the thermometer is 15.5 °C. According to the simulation (Figure 3a), the average temperature in the antennas is 228 °C. The simulation assumes that the heating in the antennas is uniform, but the heating is not actually uniform. The melting point of the Au/Si eutectic alloy is around 363 °C [25]. It indicates that the temperature in the localised region of the antennas is higher than 363 °C. If the thermometer can go though the antennas region and whilst avoiding high optical scattering from the thermometer arms, the responsivity of the bolometer could be greatly improved.

In this work, we demonstrated a waveguide-based bolometer on the a-Si platform. Compared with the bolometer on the SOI platform published in [17], the responsivity of the bolometer is improved from 1.13 %/mW to 24.62 %/mW due to the low thermal conductivity of the a-Si. The 3 dB bandwidth of the bolometer is higher than 1 kHz which is limited by the chopper in the experiment. However, in the simulation, the 3 dB bandwidth of the bolometer reaches up to 129.57 kHz. The NEP of the bolometer is 10.4 $\mu W/\sqrt{Hz}$ at 400 Hz. According to the calculation, the thermal conductance of the bolometer is 3.86 $\times\ 10^{-5}$ W/K. However, the bolometer with a thermal conductance of 2.38 $\times\ 10^{-8}$ W/K in [24] was reported. Suspension is a common method to improve this. From the SEM images and the simulation, the temperature change in the region near the antennas is ten times higher than the temperature change in the thermometer. If the thermometer can measure the temperature change in the region around the antennas, the performance of the bolometer could be greatly improved. In addition, gold, material of antennas, could be replaced by Al or TiN which is available Si foundries. The absorption in TiN antennas could be enhanced by increasing the number of antennas. Furthermore, using multiple antennas with different lengths could further increase the bandwidth of absorption. This bolometer will propel the realisation of integrated mid-infrared sensors.

All data supporting this study are openly available from the University of Southampton repository at https://doi.org/10.5258/SOTON/D1587.

FUNDING

Royal Academy of Engineering (M. Nedeljkovic fellowship RF201617/16/33); Engineering and Physical Sciences Research Council (EP/L01162X/1, EP/L021129/1, EP/N00762X/1).

DISCLOSURES

The authors declare no conflicts of interest.

REFERENCES

1. R. Soref, Nat. Photonics **4**, 495 (2010).
2. G. Z. Mashanovich *et al.*, J. Light. Technol. **35**, 624 (2017).
3. A. Schliesser *et al.*, Nat. Photonics **6**, 440 (2012).
4. M. Nedeljkovic *et al.*, Opt. Mater. Express **3**, 1205 (2013).
5. E. D. Palik, *Handbook of optical constants of solids*, vol. 3 (Academic press, 1998).
6. J. Soler Penadés *et al.*, IEEE Photonics Technol. Lett. **27**, 1197 (2015).
7. M. Nedeljkovic *et al.*, Opt. Express **25**, 27431 (2017).
8. K. Gallacher *et al.*, Opt. Express **26**, 25667 (2018).
9. M. Montesinos-Ballester *et al.*, Opt. Express **28**, 12771 (2020).
10. R. Soref, "Group iv photonics for the mid infrared," in *Silicon Photonics VIII*, , vol. 8629 (International Society for Optics and Photonics, 2013), p. 862902.
11. U. D. Dave *et al.*, Opt. Express **21**, 32032 (2013).
12. D. Thomson, L. Shen *et al.*, Opt. Express **22**, 10825 (2014).
13. M. Muneeb *et al.*, Opt. Express **24**, 9465 (2016).
14. Z. Qu *et al.*, "Waveguide integrated graphene mid-infrared photodetector," in *Silicon Photonics XIII*, , vol. 10537 (International Society for Optics and Photonics, 2018), p. 105371N.
15. L. Huang, B. Dong, X. Guo, *et al.*, ACS Nano **13**, 913 (2018).
16. A. Rogalski, "Infrared thermal detectors versus photon detectors: I. pixel performance," in *Material Science and Material Properties for Infrared Optoelectronics*, , vol. 3182 (International Society for Optics and Photonics, 1997), pp. 14–25.
17. Y. Wu *et al.*, ACS Photonics **6**, 3253 (2019).
18. Y. Wu *et al.*, "Mid-infrared silicon waveguide-based bolometer," in *2019 IEEE 16th International Conference on Group IV Photonics (GFP)*, (IEEE, 2019), pp. 1–2.
19. J.-L. Tissot, F. Rothan, C. Vedel, M. Vilain, and J.-J. Yon, "LETI/LIR's amorphous silicon uncooled microbolometer development," in *Infrared Detectors and Focal Plane Arrays V*, , vol. 3379 (International Society for Optics and Photonics, 1998), pp. 139–144.
20. S. Moon *et al.*, Int. J. Heat Mass Transf. **45**, 2439 (2002).
21. A. Yamada *et al.*, Jpn. J. Appl. Phys. **24**, 1586 (1985).
22. J. Soler Penadés *et al.*, Opt. Lett. **39**, 5661 (2014).
23. E. Aydar and I. Ekmekci, J. Therm. Sci. Technol. **32**, 63 (2012).
24. E. Mottin *et al.*, "Enhanced amorphous silicon technology for 320 x 240 microbolometer arrays with a pitch of 35 um," in *Infrared Technology and Applications XXVII*, , vol. 4369 (International Society for Optics and Photonics, 2001), pp. 250–256.
25. D. Li *et al.*, Micromachines. **8**, 158 (2017).

FULL REFERENCES

1. R. Soref, “Mid-infrared photonics in silicon and germanium,” Nat. Photonics **4**, 495 (2010).
2. G. Z. Mashanovich *et al.*, “Germanium mid-infrared photonic devices,” J. Light. Technol. **35**, 624–630 (2017).
3. A. Schliesser *et al.*, “Mid-infrared frequency combs,” Nat. Photonics **6**, 440 (2012).
4. M. Nedeljkovic *et al.*, “Silicon photonic devices and platforms for the mid-infrared,” Opt. Mater. Express **3**, 1205–1214 (2013).
5. E. D. Palik, *Handbook of optical constants of solids*, vol. 3 (Academic press, 1998).
6. J. Soler Penadés *et al.*, “Low-loss mid-infrared soi slot waveguides,” IEEE Photonics Technol. Lett. **27**, 1197–1199 (2015).
7. M. Nedeljkovic *et al.*, “Germanium-on-silicon waveguides operating at mid-infrared wavelengths up to 8.5 μm,” Opt. Express **25**, 27431–27441 (2017).
8. K. Gallacher *et al.*, “Low loss ge-on-si waveguides operating in the 8–14 μm atmospheric transmission window,” Opt. Express **26**, 25667–25675 (2018).
9. M. Montesinos-Ballester *et al.*, “Ge-rich graded sige waveguides and interferometers from 5 to 11 μm wavelength range,” Opt. Express **28**, 12771–12779 (2020).
10. R. Soref, “Group iv photonics for the mid infrared,” in *Silicon Photonics VIII,* vol. 8629 (International Society for Optics and Photonics, 2013), p. 862902.
11. U. D. Dave *et al.*, “Telecom to mid-infrared spanning supercontinuum generation in hydrogenated amorphous silicon waveguides using a thulium doped fiber laser pump source,” Opt. Express **21**, 32032–32039 (2013).
12. D. Thomson, L. Shen *et al.*, “Optical detection and modulation at 2μm-2.5 μm in silicon,” Opt. Express **22**, 10825–10830 (2014).
13. M. Muneeb *et al.*, “Iii-v-on-silicon integrated micro-spectrometer for the 3 μm wavelength range,” Opt. Express **24**, 9465–9472 (2016).
14. Z. Qu *et al.*, “Waveguide integrated graphene mid-infrared photodetector,” in *Silicon Photonics XIII,* vol. 10537 (International Society for Optics and Photonics, 2018), p. 105371N.
15. L. Huang, B. Dong, X. Guo, *et al.*, “Waveguide-integrated black phosphorus photodetector for mid-infrared applications,” ACS Nano **13**, 913–921 (2018).
16. A. Rogalski, “Infrared thermal detectors versus photon detectors: I. pixel performance,” in *Material Science and Material Properties for Infrared Optoelectronics,* vol. 3182 (International Society for Optics and Photonics, 1997), pp. 14–25.
17. Y. Wu *et al.*, “Mid-infrared nanometallic antenna assisted silicon waveguide based bolometers,” ACS Photonics **6**, 3253–3260 (2019).
18. Y. Wu *et al.*, “Mid-infrared silicon waveguide-based bolometer,” in *2019 IEEE 16th International Conference on Group IV Photonics (GFP),* (IEEE, 2019), pp. 1–2.
19. J.-L. Tissot, F. Rothan, C. Vedel, M. Vilain, and J.-J. Yon, “LETI/LIR’s amorphous silicon uncooled microbolometer development,” in *Infrared Detectors and Focal Plane Arrays V,* vol. 3379 (International Society for Optics and Photonics, 1998), pp. 139–144.
20. S. Moon *et al.*, “Thermal conductivity of amorphous silicon thin films,” Int. J. Heat Mass Transf. **45**, 2439–2447 (2002).
21. A. Yamada *et al.*, “Excimer-laser-induced chemical vapor deposition of hydrogenated amorphous silicon,” Jpn. J. Appl. Phys. **24**, 1586 (1985).
22. J. Soler Penadés *et al.*, “Suspended soi waveguide with subwavelength grating cladding for mid-infrared,” Opt. Lett. **39**, 5661–5664 (2014).
23. E. Aydar and I. Ekmekci, “Thermal efficiency estimation of the panel type radiators with cfd analysis,” J. Therm. Sci. Technol. **32**, 63–71 (2012).
24. E. Mottin *et al.*, “Enhanced amorphous silicon technology for 320 x 240 microbolometer arrays with a pitch of 35 um,” in *Infrared Technology and Applications XXVII,* vol. 4369 (International Society for Optics and Photonics, 2001), pp. 250–256.
25. D. Li *et al.*, “Investigation of au/si eutectic wafer bonding for mems accelerometers,” Micromachines. **8**, 158 (2017).